Chemistry Journals

Analytical, Inorganic, Organic, Physical, Materials Science
Hydrogen production by photocatalysis using new composites based on SiO₂ coated by TiO₂

Antonio Eduardo da H Machado [1,2], **Werick Alves Machado** [Corresp. 3]

[1] Instituto de Física, Universidade Federal de Catalão, Catalão, Goiás, Brazil

[2] Laboratório de Fotoquímica e Ciência de Materiais, Universidade Federal de Uberlândia, Uberlândia, MG, Brasil

[3] Instituto Federal de Educação, Ciência e Tecnologia do Triangulo Mineiro, Ituiutaba, Minas Gerais, Brazil

Corresponding Author: Werick Alves Machado
Email address: werickalvez@hotmail.com

In this study new TiO_2 photocatalysts core@shell type were synthesized using SiO_2 as structural support. The coating was confirmed by scanning electron microscopy and infrared spectroscopy. Adsorption isotherms revealed that the surface area of such composites is about 26% higher than pure oxide (W50). X-ray diffractograms combined with Raman spectroscopy revealed that the synthesized TiO_2 presents a structure based on the coexistence of anatase and brookite. The composite W50S50 presented the best photocatalytic performance of H_2 production, with 13.5 mmol in 5 h, corresponding to a specific rate of 32.5 mmol $h^{-1}g^{-1}$. In the reuse assays, this composite presented a good stability in the production of H_2. However, its performance presented a reduction of 23% over the reuse cycles. Considering the H_2 production in a solar simulator, W50S50 produced about 25.0 μmols, which is equivalent to 48.0 μmols $h^{-1}g^{-1}$, suggesting the good performance of this material for photocatalytic hydrogen production.

Hydrogen production by photocatalysis using new composites based on SiO_2 coated by TiO_2

Antonio Eduardo da Hora Machado[1,2], Werick Alves Machado[3]

[1] Universidade Federal de Uberlândia, Instituto de Química, Laboratório de Fotoquímica e Ciência de Materiais, Uberlândia, Minas Gerais, Brazil

[2] Universidade Federal de Catalão, Instituto de Física, Catalão, Goiás, Brazil

[3] Instituto Federal de Educação, Ciência e Tecnologia do Triangulo Mineiro (IFTM), Ituiutaba, Minas Gerais, Brazil

Corresponding Author:

Werick Alves Machado

Av. Belarmino Vilela Junqueira, S/N, CEP 38305-200, Ituiutaba, MG, Brazil

Email address: werickalvez@hotmail.com

Abstract

In this study we present new TiO_2 core@shell type photocatalysts using SiO_2 as structural support, suitable for use in photocatalytic H_2 production. The coating of SiO_2 was confirmed by scanning electron microscopy and infrared spectroscopy. Adsorption isotherms revealed that the surface area of such composites is about 26% higher than the synthesized pure oxide. X-ray diffractograms analysed in combination to Raman spectroscopy revealed that the structure of synthesized TiO_2 involves the coexistence of anatase and brookite. At lab-scale, the composite designated as W50S50 presented the best photocatalytic performance, producing 13.5 mmol of H_2 in 5 h, which corresponds to a specific rate of 32.5 mmol $h^{-1}g^{-1}$. In reuse assays, this composite presented a good stability in the production of H_2, although its performance has presented a 23% reduction in reuse cycles. In assays using a solar simulator, W50S50 produced about 25.0 μmols, equivalent to 48.0 μmols $h^{-1}g^{-1}$, suggesting for it a good performance for photocatalytic hydrogen production.

Introduction

The fast increase in global demand for energy has compromised the integrity of the environment with unprecedented speed. This is largely due to the current composition of the global energy matrix, predominantly composed of non-renewable sources such as oil, coal and natural gas (IEA, 2018). In view of this, new challenges in relation to energy generation and consumption have imposed to the society, influencing the research on energy generation, whose bias has changed towards the development of new renewable and non-polluting energy matrices. In this scenario, hydrogen (H_2) stands out as an alternative to the issues related to the energy matrix, since this gas can contribute to the production of a clean, safe and sustainable energy. However, the economically viable H_2 production still takes place through the exploitation of

43   non-renewable sources. Currently, about 48% of the global demand for this gas is met by steam

44   reform of natural gas, 28% by oil reform, 20% by coal gasification, and 4% by other processes,

45   such as electrolysis, biological and photocatalysis (Levin & Chahine, 2010). In the future, the H_2

46   produced from environmentally friendly methods, such as by photocatalytic production via water

47   splitting (Veras et al, 2017), may be an alternative way to circumvent the adverse effects of the

48   use of non-renewable sources.

49   The photocatalytic production of H_2 via water splitting can occur by a well-established

50   mechanism that involves the electronic excitation (photoactivation) of semiconductor

51   materials (photocatalysts). The photoactivation promotes the formation of charged pairs, that is,

52   positive (hole) and negative (electron) charge carriers, responsible for reduction and oxidation

53   reactions. The pathway of oxidation leads to the formation of O_2, while the reduction to the

54   formation of H_2 (Bahnemann & Schneider, 2013).

55   Among the most used materials, TiO_2 stands out due to characteristics such as

56   abundance, low toxicity, good chemical stability in a wide range of pH, photocatalytic activity,

57   photostability and insolubility in water (Santos et al, 2015; Chong et al, 2010; Kandiel et al,

58   2010; Machado et al, 2019). However, due to its relatively large band gap energy (Eg), situated

59   in the near ultraviolet, its application in photocatalysis based on the use of solar radiation ends up

60   being limited, since only 5% of the solar spectrum is in this region (Kumar & Devi, 2011). In

61   addition, other limitations are found for the application of TiO_2 as a photocatalyst, such as the

62   high recombination rate of the photogenerated charge carriers, morphology, aggregation of

63   nanoparticles, etc.

64   In this sense, the present study proposes two simultaneous fronts to minimize trends that

65   compromise TiO_2 performance, seeking to maximize the photocatalytic production of H_2: First,

66   to promote structural modifications in TiO_2 with the creation of a biphasic (anatase/brookite)

67   material. This mixture of phases tends to favor photocatalytic activity, minimizing the

68   recombination of photoinduced charge carriers, since the cathode potential of the conduction

69   band of brookite is approximately 0.14 eV lower than that of anatase (Patrocinio et al, 2015;

70   Machado & Machado, 2020). Second, the immobilization of TiO_2 on silica (SiO_2) surface, giving

71   rise to core@shell ($SiO_2@TiO_2$) type composites with different proportions of both species. The

72   immobilization of TiO_2 on SiO_2 surface tends to increase the photocatalytic activity due to the

73   lower tendency of TiO_2 to aggregate in this biphasic system (Machado et al, 2019), as well as the

74   presence of oxygen vacancies in the supported TiO_2, which can contribute to minimize the

75   recombination of photogenerated pairs (Cheng et al, 2003). Furthermore, Guo and coworkers

76   (Guo et al, 2014) suggested that the use of silica as a support tends to increase the concentration

77   of hydroxyl groups on the surface of the catalyst, making it more hydrophilic, which may favor

78   the adsorption of reagents.

79   Thus, this study aims to obtain new photocatalysts based on TiO_2, with high performance

80   in sustainable H_2 production, through the promotion of improvements in their photocatalytic

81   parameters and reducing the aggregation of TiO_2 particles. In this sense, the performance of

82   photocatalytic production of H_2 was evaluated using different biphasic composites involving

83   TiO_2 supported in SiO_2. Different characterization techniques were used in order to relate the

84 optical and morphological properties with the photocatalytic performance of these materials.
85 Therefore, the present work intends to contribute with new insights into the positive effects of
86 TiO_2 immobilization on the SiO_2 surface, aiming to potentiate the photocatalytic production of
87 H_2 and its reuse in this noble application.
88

Materials & Methods

89

Reagents

90

91   All reagents were of analytical grade, being used without prior treatment. Titanium
92 tetraisopropoxide, 97%, isopropanol, 99.5%, hexachloroplatinic hexahydrate acid, 37.5%,
93 tetraethyl orthosilicate, 98%, hydrochloric acid, 37% and sodium hydroxide, 98%, were supplied
94 by Sigma-Aldrich. Methanol, 99.8%, was supplied by Dinâmica and acetone 99.5% was
95 provided by Synth. All solutions were prepared using ultrapure water obtained through an Elix 5
96 water purification system.

Preparation of the photocatalysts

97

98   The standard photocatalyst, called W50, was obtained by the sol-gel method following a
99 description done in a previous study (Machado & Machado, 2020). This process consists in the
100 solubilization of titanium tetraisopropoxide in isopropanol at 3°C under ultrasonic stirring for 20
101 minutes, followed by its hydrolysis by the addition, by dripping, of a water /acetone 50% v/v
102 mixture, and precipitation under ultrasonic stirring. The resulting amorphous solid was washed
103 with distilled water, centrifuged, being later sintered in conventional furnace at 400 ºC for 5
104 hours.
105   The composite $SiO_2@TiO_2$ was synthesized by the sol-gel method, coating SiO_2
106 nanoparticles with TiO_2. Prior to this synthesis, SiO_2 was prepared using the Stober method
107 (Stober et al, 1968). In this method a mixture of 15 mL of deionized water, 4 mL of ammonium
108 hydroxide, 100 mL of ethanol and 3 mL of tetraethyl orthosilicate are reacted at room
109 temperature, under constant magnetic stirring for 1 h. Due the alkalinity of the resulting solution,
110 it was subsequently neutralized with a solution 5.0 mol L^{-1} of HCl. The resulting solid, SiO_2, was
111 washed using deionized water, centrifuged and dried.
112   The coating of SiO_2 by TiO_2 involved the previous dispersion of silica, in the estimated
113 amount by stoichiometric calculation, in 150 mL of 2-propanol under magnetic stirring for 1 h,
114 followed by the rapid addition of 10 mL of titanium isopropoxide to the suspension. This mixture
115 was maintained under vigorous magnetic stirring for 19 h. Subsequently, in the hydrolysis of the
116 titanium precursor, a water/acetone (50% v/v) mixture was added drop by drop to the mixture,
117 which was kept under magnetic stirring for 1 h. Finally, the resulting colloidal suspension was
118 centrifuged, being the precipitate separated and submitted to the same heat treatment provided to
119 the photocatalyst used as reference (Machado & Machado, 2020).
120   The composites were synthesized using three different proportions of SiO_2 (25%, 50%,
121 75% m/m) in relation to TiO_2, being named W50S25, W50S50 and W50S75, respectively.

Characterization of photocatalysts

122 The composites were characterized by different techniques:

123 By infrared spectroscopy (FTIR), using a Perkin Elmer MIR Frontier Single

124 spectrometer. The analysis of the samples was performed in the solid state, in the region between

125 4000 and 220 cm^{-1}, and resolution of 4 cm^{-1}, using an Attenuated Total Reflectance (ATR)

126 accessory.

127

128 The scanning electron microscopy (SEM) images and the EDS spectra were obtained

129 using a Tescan Vega 3 electronic microscope equipped with a secondary electron detector, with

130 an acceleration voltage of 5.0 kV. From the images obtained by SEM and with the help of the

131 *ImageJ* software, it was possible to calculate the particle size by randomly selecting

132 approximately 100 particles per image. From there, the histograms were built for the synthesized

133 oxides, which illustrate the average particle size distribution.

134 The surface area, porosity and pore volume measurements were performed from the

135 analysis of adsorption and desorption isotherms of N_2, using a Quantachrome equipment, model

136 NOVA touch LX1. In these assays, the samples were pretreated under flow of gaseous N_2 for

137 12h, at 120 ºC, in order to remove adsorbed gases and water. The measures were done at 77 K

138 using liquid N_2 to maintain the temperature during the analyses. The surface areas were

139 estimated using the method proposed by Brunauer, Emmett and Teller (BET) to analyze the

140 adsorption data, while the method proposed by Barrett, Joyner and Halenda (BJH) was used to

141 calculate the pore volume.

142 The X-ray diffractograms were obtained using a SHIMADZU XRD-6000 diffractometer,

143 equipped with a CuKα (λ=1.54148 nm) monochromatic font, in the $10° \leq 2\theta \leq 80°$ angular range.

144 The counting step was 0.02º and scanning speed of 0.5º/min. Finally, the spectra were refined by

145 Rietveld's method using the software FullProf (Roisnel & Rodriguez-Carvajal, 2001). As a

146 criterion of reliability and quality of refinement, the obtained S factor was less than 1.37 for all

147 photocatalysts.

148 The Raman spectra were obtained using a Horiba LabRAM HR Evolution spectrometer

149 with 600 lines/mm grid, equipped with an excitation laser at 633 nm, with power of 5 mW. The

150 spectra obtained were the result of the accumulation of eight scans in the range between 100 and

151 1000 cm^{-1}.

152 The optical absorption spectra in the diffuse reflectance mode were obtained using a

153 Shimadzu UV-1650 spectrophotometer coupled to an integrating sphere, using barium sulfate as

154 standard. These spectra were obtained at room temperature in the spectral range between 200 and

155 800 nm, being converted in terms of Kubelka-Munk's function (F(R)), thus being possible to

156 directly estimate the *band gap* (Eg) of the studied materials (Liu & Li, 2012).

Photocatalytic production of H_2

158 This was evaluated by three different approaches. In the first, the most active composite

159 was identified among the synthesized materials, which was done on bench scale experiments,

160 monitoring the production of H_2 achieved in the same time interval by each photocatalyst. In the

161 second, also on bench scale, the most efficient composite was submitted to reuse assays, in a
162 process involving four consecutive photocatalytic cycles. Finally, in a solar simulator the
163 production mediated by the most efficient composite and pure oxide (W50), was evaluated.

164   The photocatalytic system used in bench scale (Machado & Machado, 2020) is based in a
165 reactor built in borosilicate glass with total volume of 1.5 L, possessing a cooling jacket also
166 made in borosilicate glass. It is connected to a thermostatic bath, which keeps the reaction
167 medium at 20ºC. The reactor was positioned on a magnetic agitator, used to promote
168 homogenization of the aqueous suspension containing the catalyst and reactive species. A 400 W
169 high pressure (HPL-N) mercury lamp without its protective bulb was used as radiation font. The
170 photonic flow of this lamp was estimated to be 3.3×10^{-6} Einstein/s (Machado et al, 2008), and
171 irradiance equal to 100 W/m^2 in the UVA. The lamp was positioned laterally at 15 cm from the
172 reactor.

173   Before the assays of H_2 production the photocatalysts were loaded by photoreduction
174 with 0.1% m/m of Pt, obtained from a solution of hexachloroplatinic acid. The photocatalyst
175 loaded with Pt was suspended in 750 ml of a water/methanol mixture containing 20% v/v of
176 methanol, used as a sacrificial reagent. The pH of the reaction medium was adjusted to 6.2,
177 isoelectric point of TiO_2, pH at which its photocatalytic activity is favored according to studies
178 by Hoffmann et al (Hoffmann et al, 1995). For this, 0.1 mol L^{-1} solutions of HCl and NaOH were
179 used for adjustment. Before each experiment, the dissolved gases, especially oxygen, inside the
180 reactor were purged with N_2 for 5 min. Finally, with the lamp on, the photocatalytic assays were
181 started. During the reaction, aliquots of the gases produced were collected every hour, in a total
182 period of 5 hours. The gases were analyzed by gas phase chromatography using a Perkin Elmer
183 Clarus 580 chromatograph, equipped with two packed columns (porapak N 2mm and molecular
184 sieve) and a thermal conductivity detector (TCD). All experiments were carried out at least in
185 triplicate.

186   In the assays of H_2 production using a solar simulator a smaller volume reactor was used.
187 All experimental parameters such as reaction time, initial pH, photocatalyst concentration,
188 sacrifice reagent and cocatalyst were maintained proportionally equal to those employed on
189 bench scale, for comparative purposes. The solar simulator, described by Nunes (Nunes et al,
190 2019), is constituted by a reactor, also made of borosilicate glass, with an internal volume of 80
191 mL, a 300 W xenon lamp, used as radiation font, and an AM1.5 filter, which simulates solar
192 conditions after radiation passes through 1.5 times the atmospheric mass. This is equivalent to
193 the direct incidence of solar radiation on earth's surface, with a deviation of 48.2º from the angle
194 of zenith (Honsber & Bowden, 2019). The reactor cooling system was connected to a
195 thermostatic bath to keep the reaction medium at 20 ºC. During the reactions, the content inside
196 the reactor was maintained under stirring. The reactor was positioned at 15 cm from the radiation
197 source, being exposed to an irradiance of 20 W/m^2 in the UVA.

198   For comparative purposes, since different photocatalytic systems were used, in addition
199 to the amount, in mols, of produced H_2, the results were expressed in terms of specific rate of H_2
200 production (SRHP) (Machado et al, 2019; Lin & Shih, 2016),

201
$$SRPH = \frac{n}{t\,m}$$

202   where n is the number of mols of H_2, obtained by integration in the interval between 4 and 5 h; t
203   is the time of reaction; m is the mass of catalyst (g).

204

Results and Discussion

206   **Characterizations**

207   Figure 1 presents the FTIR spectra of pure TiO_2, SiO_2, and of the TiO_2/SiO_2 composites
208   (W50S25, W50S50 and W50S75). It is possible to distinguish three typical vibrations related to
209   pure SiO_2: bands at 438 and 803 cm^{-1} and a band centered at 1050 cm^{-1} related, respectively, to
210   bending and symmetrical and asymmetric stretching of Si-O-Si, and a secondary vibration at 960
211   cm^{-1} related to silanol groups (Si-OH) (Panwar et al, 2016; Kermadi et al, 2015). For pure TiO_2,
212   three characteristic bands are observed: a wide and intense at 403 cm^{-1} and two more subtle, at
213   530 and 730 cm^{-1}, both related to Ti-O-Ti stretching (Mohamed et al, 2015). The composites
214   present the two most intense bands of the respective oxides, with small displacements: a band
215   centered at 1102 cm^{-1}, associated to silica, and a band at 403 cm^{-1}, related to TiO_2.

216

217   Figure 1 - Infrared transmission spectra obtained for the synthesized oxides.

218

219   The low signal intensity referring to the silanol groups in the composites proves the silica
220   coating by TiO_2. These groups, present on the silica surface, assists in the stability of metal
221   charges through the Si-O-M bonds, favoring the dispersion of TiO_2 over the support (Almeida et
222   al 2004; Chen et al, 2018). It is also observed that composites with higher concentrations of SiO_2
223   have a more intense band centered at 960 cm^{-1} due to silica not covered by TiO_2.
224   The Si-O-Si vibration, in general at 1050 cm^{-1}, is slightly shifted to higher frequencies
225   (approximately 1102 cm^{-1}) due to calcination of these materials at high temperature, suggesting
226   the strengthening of the Ti-O bond (Kermadi et al, 2015). In general, in all spectra it was
227   possible to observe the presence of two relatively wide bands at 1636 and 3360 cm^{-1}, related to
228   O-H vibration of water molecules chemically and physically adsorbed on the surface of the
229   photocatalyst (Poo et al, 2019).
230   In Figures S1 to S5, Supplementary Material, the images obtained by SEM are shown.
231   They are accompanied by their EDS spectra and histograms, that illustrate the average particle
232   size distribution of photocatalysts (Table 1). From the analysis of the figures, it is observed that
233   the particles of pure TiO_2 have a dense aspect, with irregular spherical shape and average particle
234   sizes ranging from 0.2 to 1.0 μm. Pure silica presents particles of regular spherical shape, with
235   uniform average size. However, for them there is a tendency to aggregation, giving rise to bulky
236   clusters of SiO_2. For the studied composites, when compared to the W50, the reduction of the
237   average particle size between them is evident, and this occurs as consequence of the coating of
238   SiO_2 by TiO_2 (Lin et al, 2013). For composite W50S75 it is verified through the analysis of the

239 histogram, the existence of excess of SiO_2, with the presence of particles with average diameter
240 of 0.2 μm, in addition to a considerable increase in the aggregation state.
241
242   Table 1- Morphological parameters related to the synthesized materials.
243
244   The isotherms, Figure S6 - Supplementary Material, suggest that the photocatalysts under
245 study are type IV, characterized by being mesoporous, with average pore diameter between 2 and
246 50 nm, corroborating with the average pore diameter values, as displayed in Table 1. The profile
247 of hysteresis are similar to type H2, which correspond to complex mesoporous structures, in
248 which the distribution of pore size and shape is not well defined. Silica, in turn, presented type I
249 isotherm and hysteresis characteristics of microporous materials, composed by agglomerates of
250 spheroidal particles with close size distribution (IUPAC, 1985). Due to this, it is observed that
251 the silica hysteresis loop does not close a typical behavior of materials with very narrow pores or
252 bottle-shaped pores. This evidences the low average pore size, that prevents the diffusion of
253 adsorbed N_2 (Tang et al, 2015).The observed porosity also corroborates with the formation of the
254 composite since the immobilization of TiO_2 on the silica surface leads to the formation of new
255 pores, resulting in increased porosity and consequent increase in the surface area (Salgado &
256 Valentini, 2015). The composite W50S50 presented the highest porosity among the synthesized
257 composites, which ensures greater adsorption of reagents on its surface, consequently increasing
258 its photocatalytic action.
259   By analyzing the diffractograms shown in Figure 2, and confronting with information
260 reported in literature (Machado & Machado, 2020; Neto et al, 2017) and with the JCPDS 21-
261 1272 (anatase) and 29-1360 (brookite) crystallographic files, it is possible to observe the
262 coexistence of two crystalline phases in all the synthesized oxides, being anatase the main phase
263 and brookite the secondary. It is worth mentioning the similarity of the diffraction profiles of
264 these materials, with emphasis on the well-defined diffraction peaks for the uncoated material
265 (W50), suggesting a significant increase in the crystallinity as a consequence of the heat
266 treatment applied during the synthesis (El-Sheikh et al, 2017). On the other hand, it is observed
267 that the intensity of the peaks decreases as the concentration of silica increases, indicating a
268 decrease in the crystallinity of the composites, consequence of the non-crystallinity of SiO_2
269 (Machado et al, 2019).
270
271   Figure 2 - X-ray diffractogram for the synthesized oxides.
272
273   From the diffractograms, it was possible to obtain, through Rietveld refinement, the
274 proportion of crystalline phases, average size and the average deformation of the crystallite for
275 synthesized species, Table 2. The diffractograms, accompanied by their respective calculated
276 diffraction profiles, experimentally obtained profile, residual curves and Bragg diffraction
277 adjusted by the Rietveld method, can be viewed in Figure S7 - Supplementary Material. The
278 reliability factors of refinement are shown in Table T1.

279
280   Table 2- Percentage of crystalline phase, size and average maximum crystallite
281   deformation, obtained from Rietveld refinement.
282
283   The presence of brookite phase in the composites was verified in the oxide designated as
284   W50, synthesized in a previous study (Machado & Machado, 2020). This involved the use of
285   water/acetone mixtures to control the hydrolysis of titanium tetraisopropoxide. The presence of
286   acetone during the synthesis affects the organization of the critical nuclei formed from the
287   oligomeric network generated from titanates, which tends to favor the formation of the brookite
288   phase (Machado & Machado, 2020). On the other hand, the addition of silica during the
289   synthesis of the materials evaluated in the present study apparently did not influence the
290   formation of any crystalline phase.
291   In the present study, the composite W50S50 presented the highest percentage of brookite
292   among the synthesized materials - an increase of 25% compared to pure oxide. As shown in
293   Table 2, the other composites showed similar proportions between the crystalline phases. The
294   average crystalline size of the composites for both crystalline phases decreased with increasing
295   silica concentration in the structure. A more expressive reduction was observed for composite
296   W50S75, which presented contraction of the anatase phase greater than five times in comparison
297   with pure oxide. This suggests that the presence of silica should inhibit the growth and surface
298   diffusion processes of TiO_2 nanoparticles due the curvature of the silica surface and the
299   formation of interfacial bonds between oxides (Machado et al, 2019; Li et al, 2013). It was also
300   found that the behavior of the mean maximum deformation was inversely proportional to the
301   average crystallite size, since the formation of interfacial bonds tends to compromise the
302   integrity of the anatase and brookite crystals. According to Staykov (Staykov et al, 2017), the
303   strong Si-O-Ti bonds at the composite interface tensions the crystalline network of TiO_2 and can
304   change the coordination sphere of Ti^{4+} from six to five coordinated O^{2-}. Thus, the increase in
305   silica concentration in the TiO_2 structure leads to an increase in tension in the crystalline
306   network, which tends to increase the average deformation of the material (Staykov et al, 2017).
307   As well as the diffractograms obtained by X-ray diffraction, the Raman spectra shown in
308   Figure 3 also evidence the biphasic composition of these photocatalysts. The active modes
309   corresponding to the anatase phase are located at 144 cm^{-1} (E_g), 197 cm^{-1} (E_g), 399 cm^{-1} (B_{1g}),
310   513 cm^{-1} (A_{1g}), 519 cm^{-1} (B_{1g}) and 639 cm^{-1} (E_g) (Staykov et al, 2017; Sekiya et al 2001). For the
311   analyzed samples, five of these main bands are observed in the following regions: 144 cm^{-1} (E_g),
312   198 cm^{-1} (E_g), 399 cm^{-1} (B_{1g}), 519 cm^{-1} (B_{1g}) and 640 cm^{-1} (E_g). The mode A_{1g} at 513 cm^{-1} was
313   probably not visualized due to its low intensity in combination with the overlay of the mode B_{1g},
314   more intense and close to 519 cm^{-1} (Iliev et al, 2013; Fang et al, 2015). In the insert in Figure 3,
315   between 200 and 500 cm^{-1} four subtle bands attributed to the brookite phase are observed in 245
316   cm^{-1} (A_{1g}), 321 cm^{-1} (B_{1g}), 365 cm^{-1} (B_{2g}) and 452 cm^{-1} (B_{3g}). The band of higher intensity for
317   the phase brookite is close to 153 cm^{-1} (A_{1g}). It may be overlapthed with the anatase band, much
318   more intense, at 144 cm^{-1} (E_g), which should influence the wider width of this Raman mode (Yin

319 et al, 2007; Hellawell et al, 2015). In figure S8, Supplementary Material, the Raman spectrum of
320 pure silica is shown, in the spectrum well-defined Raman bands between 200 and 600 cm^{-1} are
321 not observed, but it has a single wide band between 1000 and 2250 cm^{-1}, characteristic of
322 tetrahedrons SiO_4 jitters typical of amorphous SiO_2 as shown by X-ray diffraction (Shoo et al,
323 2009).
324
325 Figure 3 - Raman spectra of the synthesized materials. Insert: bands at 245 cm^{-1}, 321 cm^{-1}, 365
326 cm^{-1} and 452 cm^{-1}, attributed to brookite phase.
327
328 The estimated values for Eg from the diffuse reflectance spectra, Figure 4, are 3.25 eV
329 for W50, 3.32 eV for W50S25 and W50S50, and 3.35 eV for W50S75. These results agree with
330 the reported in the literature, which suggests an Eg of approximately 3.2 eV for pure TiO_2 (Neto,
331 et al 2017). As observed above, the estimated value for E_g for the synthetized composites is
332 slightly higher, probably due the formation of interfacial bonds (Si-O-Ti), which tends to change
333 the electronic frontier states. In addition, it is known that the electronic properties of particles
334 tend to change significantly with the reduction of their size due the occurrence of quantum
335 confinement, which tends to increase the Eg value (Kumar & Devi, 2011). As the results
336 obtained by TEM and XRD suggest, composites that have higher silica content in their
337 composition have smaller particulate and crystalline sizes and consequently higher Eg values. It
338 is worth noting that amorphous silica possesses Eg higher than 8.0 eV (Machado et al, 2019;
339 Nekrashevich & Gritsenko, 2014).
340
341 Figure 4 - Diffuse reflectance spectra in an enlarged scale vs. Kubelka-Munk's function,
342 combined to linear segments used in determining E_g values. Insert: Diffuse reflectance spectra,
343 without magnification, for the synthesized materials.
344

345 **Photocatalytic production of H_2 in a bench-scale**

346 Being known the morphological and optical properties of the materials presented in this
347 work, the photocatalytic activity regarding the photocatalytic production of hydrogen was
348 evaluated through bench-scale tests under UV-vis irradiation. After defining the most efficient
349 photocatalyst, its potential for reuse was evaluated. Following, the performance of these same
350 composites in the production of H_2, compared to that of pure oxide, was evaluated using a solar
351 simulator.
352 It is observed, from Figure 5, that the synthesized composites obtained better
353 performance in the production of H_2 than the pure oxide (W50), with the exception of W50S75,
354 responsible for the lowest productivity of the set, about 20% less than that achieved using the
355 W50. As observed in SEM images along with histograms and EDS spectra, the poor performance
356 of the W50S75 should be attributed to excess of free silica, photocatalytically inert, in its
357 composition. The most efficient composite, W50S50, produced approximately 13.5 mmols of H_2
358 in 5 h of reaction, performance 40% higher than that obtained using the W50, which produced
359 about 9.6 mmols in the same time interval. Using the W50S25, a production of 11.0 mmols was
360 achieved, a value approximately 14% higher than that obtained using pure oxide. It is noteworthy

361 that H_2 production tests were also performed using pure silica associated with platinum and
362 platinum powder. However, as expected, no H_2 production was obtained in both situations, in 5
363 hours of reaction.
364
365 Figure 5 - Photocatalytic production of hydrogen vs. Reaction time for the materials under study.
366
367   The more efficient production of H_2 by W50S50 was favored by the higher
368 anatase/brookite heterophasic crystalline composition, possibly due the more negative cathode
369 potential of the conduction band of the brookite phase. This tends to favor the reduction of
370 protons during the production of H_2 (Patrocinio et al, 2015; Machado & Machado, 2020)Tay et
371 al, 2013). Morphological aspects, such as the high surface area, high porosity and lower particle
372 size, should also contribute to potentiate the photocatalytic activity of this oxide.
373   In a previous study published by us (Machado et al, 2019) 5.5 mmols of H_2 were
374 produced in 5 h of reaction, which is equivalent to a SRHP of 13.6 mmol g^{-1} h^{-1}, using a
375 TiO_2/SiO_2 composite based on TiO_2 100% anatase, and approximate composition of 80% of TiO_2
376 and 20% of SiO_2. The increase in photocatalytic performance in terms of H_2 production using the
377 biphasic composite W50S50 is indisputable since, using these same experimental conditions, it
378 was achieved, in the present study, a SRHP approximately two and a half times larger. Regarding
379 a comparison of the photocatalytic action of W50S50 and the other catalysts evaluated in the
380 present study with other catalysts reported in the literature, developed for the same purpose, it is
381 worth mentioning the work of Lin and coworkers (Lin et al, 2011) who evaluated the efficiency
382 of Nb_2O_5 combined with different metals as cocatalyst. They used a halogen lamp of 400W as
383 radiation font and aqueous solutions containing 20% of methanol. Under the best conditions,
384 using platinum as cocatalyst, a SRHP of 4.6 mmol $h^{-1}g^{-1}$ was reached. In the present study, using
385 W50S50 as catalyst, a SRHP seven times higher was achieved. In a study involving the
386 photodeposition of CuO on the surface of ZnO, Liu and coworkers obtained, under the best
387 conditions, a SRHP of 1.7 mmol $h^{-1}g^{-1}$ (Liu et al, 2011), using the catalyst suspended in aqueous
388 solutions containing 10% v/v of methanol and irradiated by a 400W mercury vapor lamp. Also,
389 using the composite W50S50 as catalyst, we obtained a much higher SRHP.

390 **Potential for reuse of W50S50 for H_2 production in a bench-scale**

391   The evaluation of the potential of reuse of the photocatalyst consisted of measuring the
392 reproducibility of catalytic action of the W50S50 by repetitive tests, called cycles, using the same
393 initial conditions applied to the system, only with the pH of the medium being adjusted at the
394 beginning of each additional cycle. The reuse assays were performed in sequence of four
395 photocatalytic cycles, each involving 5 hours of reaction. The first cycle was equivalent to the H_2
396 production test carried out in a single cycle of five hours.

397   Figure 6 shows the very good stability in H_2 production in each cycle, which maintains,

398 individually per cycle, a regular upward pattern, within 20 h of the tests. However, there is a subtle

399 decrease in production in each cycle when compared to the previous cycle.

400

401   Figure 6 - Amount of H_2 produced by the photocatalyst W50S50 in four cycles of reuse.

402

403   Table 3, that contains the compilation of Figure 6 data, shows the number of mols of H_2

404 produced in each cycle of reuse together with the respective SRHP. There was a reduction of

405 approximately 18% in the production of H_2 between the first and last cycle. The SRHP of 32.0

406 mmol $h^{-1}g^{-1}$ reached in the first cycle was reduced to 31.0 mmol $h^{-1}g^{-1}$ in the second cycle, an

407 almost equivalent value, whereas in the last cycle this value was reduced to 26.0 mmol $h^{-1}g^{-1}$. This

408 can be attributed to the exhaustion of the sacrificial reagent stock. Methanol, when oxidized, tends

409 to become formaldehyde and formic acid (Mcmurry, 2011). The pH at the end of each cycle was

410 monitored in order to qualitatively verify the formation of formic acid during the reaction. In fact,

411 it was observed that the pH was reduced during the reuse cycles. From the third cycle, a significant

412 reduction in the pH as well as of SRHP is evident.

413

414 Table 3 - Amount, in mmol of H_2, produced, specific rate of H_2 production (SRHP), initial and

415  final pHs for each cycle in the reuse assay. Photocatalytic production of H_2 in solar simulator.

416

417   Figure 7 shows the amount of H produced by each photocatalyst using the solar

418 simulator, accompanied by their respective standard deviations. It is observed that the compound

419 W50S50 maintains a high performance in comparison with pure oxide. Similar to that observed

420 in bench-scale production, the production using this composite is also approximately 40%

421 higher. Despite the electronic absorption by this material is subtly shifted to the region of higher

422 energies (Figure 4), its production in five hours of reaction was 25 μmols against 18 μmols using

423 the pure oxide, which is equivalent to, respectively, SRHPs of 66.6 and 48.0 μmol $g^{-1}h^{-1}$. Thus, it

424 is clear that the synergism between SiO_2 and TiO_2 tends to favor the photocatalytic activity in the

425 production of H_2. Even with the subtle hypsochromic displacement observed, in the mediation of

426 the photocatalytic process by the solar simulator using the composite, the result was superior

427 than that achieved using pure oxide.

428

429 Figure 7 - Amount of H_2, in μmols, produced by the photocatalysts W50 and W50S50, using a

430                solar simulator

431

432   Due the amount of H_2 produced using the solar simulator and the detection limit of the

433 gas chromatograph, in this experiment it was not possible to monitor the temporal evolution of

434 H_2. In this case, only aliquots collected with five hours of reaction were analyzed, and each

435 experiment was replicated at least three times.

436

437 **Conclusions**

438   Infrared and dispersive energy spectra in addition to scanning electron microscopy
439   images confirmed the coating of SiO_2 nanoparticles by TiO_2. The images obtained by scanning
440   electronic microscopy also revealed that the spherical shape of the composite nanoparticles
441   present high regularity most likely due the immobilization of TiO_2 on Stober' sílica surface. It is
442   also worth mentioning that the average size of the composite nanoparticles was uniform with a
443   slight reduction compared to the size of the pure oxides that constitute them.

444   The N_2 adsorption and desorption isotherms demonstrated that the synthesized
445   composites are mesoporous materials with mean pore sizes between 3 and 4 nm with
446   approximately 20% of porosity, but without defined distribution and form. The surface area of
447   these composites, calculated by employing the BET method, is approximately 26% higher in
448   relation to pure oxide (W50).

449   The difratograms, together with the Raman spectra, revealed crystalline materials with
450   the coexistence of anatase, as the main phase, and brookite. In addition, the diffractograms
451   refined by the Rietveld method demonstrated that the composites maintained a proportion of
452   about 75 and 25%, respectively of anatase and brookite. The average size of the crystallites has
453   changed due the synthesis. In both crystalline phases there was a reduction in the average size
454   with the increase of silica concentration in the structure. This suggests that the presence of silica
455   inhibits the growth and surface diffusion processes of TiO_2 nanoparticles, probably due the
456   curvature of the silica surface and formation of interfacial bonds between oxides.

457   The *band gap* energies estimated for the composites were slightly higher than that shown
458   by standard oxide (3.2 eV). This should possibly be related to the mixture of electronic states of
459   both materials (SiO_2@TiO_2), since Stober's amorphous silica presents an Eg higher than 8.0 eV.

460   In the photocatalytic assays of H_2 production on bench scale, the composites, in general,
461   showed excellent photocatalytic performance, probably due the lower mobility of TiO_2 in view
462   of its fixation to silica surface. The composite W50S50 proved to be the most efficient, since
463   with five hours of reaction it was achieved the production of approximately 13.5 mmol of H_2, a
464   value 40% higher than that achieved using pure TiO_2. The good performance of this composite
465   should be related to its morphological parameters, such as its high surface area, crystallite size,
466   particle size smaller than other composites, and mainly to its higher heterophasic crystalline
467   composition, since the cathode potential of brookite phase conduction band is more negative,
468   favoring the reduction of protons in the production of H_2. Silica, which does not present
469   photocatalytic activity, did not produce H_2.

470   In the reuse assays of W50S50, it showed excellent stability during the production of H_2.
471   However, there was a decrease of 23% between the first and the last cycle, attributed to the
472   exhaustion of the stock of sacrificial reagent.

473   In the photocatalytic production of H_2 using a solar simulator, the performance of
474   W50S50 remained 40% superior to that obtained using the pure oxide. In five hours of reaction,
475   this composite produced 25 μmols against 18 μmols using the pure oxide, which equates to a
476   SRHP of, respectively, 66.6 and 48.0 μmol $g^{-1}h^{-1}$.

477

Acknowledgements

The authors thank to Institute of Physics of Uberlandia Federal University (UFU) for the RAMAN spectrum measures, to Research Group in Inorganic Materials (UFU) for the BET measures, and to Institute of Chemistry of Uberlandia Federal University for the scanning electron microscopy images.

References

Almeida, R. M.; Marques, A. C.; Pelli, S.; Righini, G. C.; Chiasera, A.; Mattarelli, M.; Tosello, C.; Gonçalves, M. C.; Portales, H.; Chaussedent. S.; Ferrari, M.; Zampedri, L. 2004. Spectroscopic assessment of sílica-titania and sílica-hafnia planar waveguides. *Philosophical Magazine*, v. 84, n. 13-16, p.1659-1666. https://doi.org/10.1080/14786430310001644459

B. N. Nunes, A. O. T. Patrocinio, D. F. Bahnemann. 2019. Influence of the preparation conditions on the morphology and photocatalytic performance Pt-modified hexaniobate composites, *Journal of Physics: Condensed Matter*, v.31, p. 394001. https://doi.org/10.1088/1361-648X/ab2c5e

Bahnemann, D. W.; Schneider, J. 2013. Undesired role of sacrificial reagents in photocatalysis. *The Journal of Physical Chemistry Lerrers,* v. 4, n. 20, p. 3479-3483. https://doi.org/10.1021/jz4018199

Chen, J.; Hu, Y.; Cai, A.; Cheng, T.; Wu, Z.; Liu, H.; Bao, X.; Yuan, P. 2018. The mesopore-elimination treatment and silanol-groups recover for macroporous silica microspheres and its application as an eficiente support for polystryrene hydrogenation. *Catalysis Communications*, v. 111, p. 75-79. https://doi.org/10.1016/j.catcom.2018.04.001

Cheng, P.; Zheng, M.; Jin, Y.; Huang, Q. Gu, M. 2003. Preparation and characterization of silica-doped titania photocatalyst through sol–gel method. *Materials Letters*, v. 57, n. 20, p. 2989-2994. https://doi.org/10.1016/S0167-577X(02)01409-X

Chong, M. N.; Jin, B.; Chow, C. W. K.; Saint, C. 2010. Recent developments in photocatalytic water treatment technology: A review. *Water Research*, v. 44, n. 10, p. 2997-3027. https://doi.org/10.1016/j.watres.2010.02.039

El-Sheikh, S. M.; Khedra, T. M.; Hakkib, A.; Ismaila, A. A.; Badawy, W. A.; Bahnemann, D. W. 2017. Visible light activated carbon and nitrogen co-doped mesoporous TiO2 as efficient photocatalyst for degradation of ibuprofen. *Separation and Purification Technology,* v. 173, p. 258-268. https://doi.org/10.1016/j.seppur.2016.09.034

Fang, H.; Zhang, C. X.; Liu, L.; Zhao, Y. M.; Xu, H. J. 2015. Recyclable threedimensional Ag nanoparticle-decorated TiO2 nanorod arrays for surface-enhanced Raman scattering. *Biosensors & Bioelectronics,* v. 64, p. 434-441. https://doi.org/10.1016/j.bios.2014.09.053

Guo, N.; Liang, Y.; Lan, S.; Liu, L.; Ji, G.; Gan, S.; Zou, H.; Xu, X. 2014. Uniform TiO_2–SiO_2 hollow nanospheres: Synthesis, characterizationand enhanced adsorption– photodegradation of azo dyes and phenol. *Applied Surface Science*, v. 305, p. 562-574. http://dx.doi.org/10.1016/j.apsusc.2014.03.136

Hoffmann, M. R.; Martin, S. T.; Choi, W.; Bahnemann, D. W. 1995. Environmental Applications of Semiconductor Photocatalysis. *Chemical Reviews,* v. 95, n. 1, p. 69-96. https://doi.org/10.1021/cr00033a004

Honsber, C.; Bowden, S. 2019. *Pveducation*, 2-Properties of sunlight, Air Mass. Available at: https://www.pveducation.org/pvcdrom/properties-of-sunlight/air-mass. (accessed 08 june 2022)

IEA, International Energy Agency 2018. Data and Statistics. Available at: https://www.iea.org/data-and-statistics. (accessed 07 june 2022)

Iliev, M. N.; Hadjiev, V. G.; Litvinchuck, A. P. 2013. Raman and infrared spectra of brookite (TiO2): Experiment and theory. *Vibrational Spectroscopy,* v. 64, p. 148-152. https://doi.org/10.1016/j.vibspec.2012.08.003

IUPAC. 1985. Comission on Colloid and Surface Chemistry Including Catalysis. *Pure and Applied Chemistry*. v. 57, n. p. 603. http://dx.doi.org/10.1351/pac198557040603

J, Mcmurry. 2011, Química Orgânica, cambo. *Cengage Learning*.7ª ed. Norte-Americana. Cornell University.

J. Hellawell, C. Ballhaus, C. T. Gee, E. G. Mustoe, J. T. Nagel, R. Wirth, J. Rethemeyer, F. Tomaschek, T. Geiler, K. Greef, T. Mansfeldt. 2015. Incipient silicification of recent conifer wood at a Yellowstone hot spring. *Geochimica et Cosmochimica Acta*, v. 149, p. 79-87. https://doi.org/10.1016/j.gca.2014.10.018

J. Tang, M. Yang, F. Yu, X. Chen, L. Tan, Ge. Wang. 2017. 1-Octadecanol@hierarchical porous polymer composite as a novel shape-stability phase change material for latent heat thermal energy storage. *Applied Energy*. **187**p. 514-522. https://doi.org/10.1016/j.apenergy.2016.11.043

559 **Kandiel, T. A., Feldhoff, A., Robben, L., Dillert, R., Bahnemann D. W. 2010.**
560 Tailored Titanium Dioxide Nanomaterials: Anatase Nanoparticles and Brookite Nanorods
561 as Highly Active Photocatalysts. *Chemistry of Materials*, v. 22, n. 6, p. 2050-2060.
562 https://doi.org/10.1021/cm903472p

564 **Kermadi, S.; Agoudjil, N.; Sali, S.; Zougar, L.; Boumaour, M.; Broch, L.; En
565 Naciri, A.; Placido, F. 2015.** Microstructure and optical dispersion characterization of
566 nanocomposite sol–gel TiO2–SiO2 thin films with different compositions.
567 *Spectrochimica Acta Part A: Molecular and Biomolecular Spectroscopy*, v. 145, p. 145,
568 145. http://dx.doi.org/10.1016/j.saa.2015.02.110

570 **Kumar, S. G.; Devi, L. G. 2011.** Review on Modified TiO_2 Photocatalysis under
571 UV/Visible Light: Selected Results and Related Mechanisms on Interfacial Charge
572 Carrier Transfer Dynamics. *Journal of Physical Chemistry A*, v. 115, n. 46, p. 13211-
573 13241. https://doi.org/10.1021/jp204364a

575 **Levin, D. B.; Chahine, R. 2010.** Challenges for renewable hydrogen production from
576 biomass. *International Journal of Hydrogen Energy,* v. 35, n. 10, p. 4962-4969.
577 https://doi.org/10.1016/j.ijhydene.2009.08.067

579 **Li, A.; Jin, Y.; Muggli, D.; Pierce, D. T.; Aranwela, H.; Marasinghe, G. K.;
580 Knutson, T.; Brockmana, G.; Zhao, J. X. 2013.** Nanoscale effects of silica particle
581 supports on the formation and properties of TiO_2 nanocatalysts. *Nanoscale*, v. 5, p. 5854-
582 5862. https://doi.org/10.1039/c3nr01287e

584 **Lin, H. H.; Yang, H. C.; Wang, W. L. 2011.** Synthesis of mesoporous Nb_2O_5
585 photocatalysts with Pt, Au, Cu and NiO cocatalyst for water splitting. *Catalysis Today*, v.
586 174, p. 106-113. https://doi.org/10.1016/j.cattod.2011.01.052

588 **Lin, H. Y.; Shih, C. Y. 2016.** Efficient one-pot microwave-assisted hydrothermal
589 synthesis of M (M=Cr, Ni, Cu, Nb) and nitrogen co-doped TiO2 for hydrogen production
590 by photocatalytic water splitting. *Journal of Molecular Catalysis A: Chemical,* v. 411, p.
591 128-137. https://doi.org/10.1016/j.molcata.2015.10.026

593 **Liu, C. S.; Li, F. 2012.** Natural path for more precise determination of band gap by
594 optical spectra. *Optics Communications,* v. 285, n. 12, p. 2868-2873.
595 https://doi.org/10.1016/j.optcom.2012.02.049

597 **Liu, Z.; Bai, H.; Xu, S.; Sun, D. D. 2011.** Hierarchical CuO/ZnO "corn-like"
598 architecture for photocatalytic hydrogen generation. *International Journal of Hydrogen*
599 *Energy*, v. 36, p. 13473-13480. https://doi.org/10.1016/j.ijhydene.2011.07.137

600

601 **Machado, A. E. H.; Franca, M. D.; Velani, V.; Magnino, G. A.; Velani, H. M. M.;**
602 **Freitas, F. S.; Muller, P. S.; Sattler, C.; Schmucker, M. 2008**. Characterization and
603 evaluation of the efficiency of TiO2/zinc phthalocyanine nanocomposites as
604 photocatalysts for wastewater treatment using solar irradiation. *International Journal of*
605 *Photoenergy*, Article ID 482373. http://dx.doi.org/10.1155/2008/482373

606

607 **Machado, W. A.; Alves, H. O.; Machado, A. E. H. 2019.** Synthesis and Evaluation of
608 the Photocatalytic Activity of Nanostructured Composites Based on SiO_2 Recovered by
609 TiO_2. *Orbital: The Eletronic Journal of Chemistry*, v. 11, n. 2, p. 83-90.
610 http://dx.doi.org/10.17807/orbital.v11i2.1347

611

612 **Machado, W. A.; Machado, A. E. H. 2020.** Characterization and evaluation of the
613 photocatalytic activity of oxides based on TiO_2 synthesized by hydrolysis controlled by
614 the use of water/acetone mixtures. *PeerJ Materials Science*, 2, e11.
615 https://doi.org/10.7717/peerj-matsci.11

616

617 **Mohamed, M. M.; Osman, G.; Khairou, K. S. J. 2015.** Fabrication of Ag nanoparticles
618 modified TiO_2–CNT heterostructures for enhanced visible light photocatalytic
619 degradation of organic pollutants and bactéria. *Journal of Evironmental Chemical*
620 *Engineering,* v. 3, p. 1847-1859. http://dx.doi.org/10.1016/j.jece.2015.06.018

621

622 **Nekrashevich, S.; Gritsenko, V. 2014.** Electronic structure of silicon dioxide (a review).
623 *Physics of the Solid State*, v. 56, p. 207-222.
624 https://doi.org/10.1134/S106378341402022X

625

626 **Neto, J. O. M; Bellato, C. R; Souza, C. H. F; Silva, R. C; Rocha, P. A. 2017.**
627 Synthesis, Characterization and Enhanced Photocatalytic Activity of Iron Oxide/Carbon
628 Nanotube/Ag-doped TiO_2 Nanocomposites**.** *Journal of the Brazilian Chemical Society*, v.
629 28, n. 12, p. 2301-2312. https://dx.doi.org/10.21577/0103-5053.20170081

630

631 **Panwar, K.; Jassal, M.; Agrawal, A. K. 2016.** TiO_2–SiO_2 Janus particles with highly
632 enhanced photocatalytic activity. *RSC Advances*, v. 6, p. 92754-9276.
633 http://dx.doi.org/10.1039/c6ra12378c

634

635 **Patrocinio, A. O. T.; Schneider, J.; França, M. D.; Santos, L. M.; Machado, A. E.**
636 **H.; Bahnemann, D. W. 2015.** Charge carrier dynamics and photocatalytic behavior of
637 TiO_2 nanopowders submitted to hydrothermal or conventional heat treatment. *RSC*
638 *Advances*, v. 5, n. 86, p. 70536-70545. https://doi.org/10.1039/C5RA13291F

639

640   **Poo-Arporn, Y.; Kityakarn, S.; Niltharach, A.; Smith, M. F.; Seraphin, S.; Worner,**
641   **M.; Worayingyong. 2019.** Photocatalytic oxidation of thiophene over cerium doped
642   TiO2 thin film. *Meterials Science in Semicondutctor Processing.* v, 93, p. 21-27.
643   https://doi.org/10.1016/j.mssp.2018.12.025

645   **Roisnel, T.; Rodriguez-Carvajal, J. 2001.** WinPLOTR: A Windows Toll for Powder
646   Diffraction Pattern Analysis. *Materials Science Forum*, v. 378, p. 118-123.
647   https://doi.org/10.4028/www.scientific.net/MSF.378-381.118

649   **Sahoo, S.; Arora, A. K.; Sridharan, V. 2009.** Raman Line Shapes of Optical Phonons
650   of Different Symmetries in Anatase TiO2 Nanocrystals. *Journal of Physical Chemistry C*,
651   v. 113(39), p. 16927-16933. https://doi.org/10.1021/jp9046193

653   **Salgado, B. C. B.; Valentini, A. 2015.** Síntese e Desempenho Fotocatalítico de Esferas
654   Macroporosas de Sílica Revestidas com Dióxido de Titânio. *Revista Virtual de Química*,
655   v. 7, n. 6, p. 2291-2310. https://doi.org/10.5935/1984-6835.20150136

657   **Santos, L. M.; Machado, W. A.; França, M. D.; Borges, K. A.; Paniago, R. M.;**
658   **Patrocínio, A. O. T.; Machado, A. E. H. 2015**. Structural characterization of Ag-doped
659   TiO2 with enhanced photocatalytic activity, *RSC Advances*, v. 5, p. 103753-103759.
660   https://doi.org/10.1039/C5RA22647C

662   **Sekiya, T.; Ohta, S.; Kamei, S.; Hanakawa, M.; Kurita, S. 2001.** Raman spectroscopy
663   and phase transition of anatase TiO2 under high pressure. *Journal of Physics and*
664   *Chemistry of Solids,* v. 62, n. 4, p. 717-721. https://doi.org/10.1016/S0022-
665   3697(00)00229-8

667   **Staykov, A.; Neto-Ferreira, E. P.; Cruz, J. M. Y. S.; Ullah, S; Filho-Rodrigues, U. P.**
668   **2017.** The stability of titania-silica interface. *International Journal Quantum Chemistry,*
669   v. 118. https://doi.org/10.1002/qua.25495

671   **Stöber, W.; Fink, A.; Bohn, E. 1968.** Controlled growth of monodisperse silica spheres
672   in the micron size range. *Journal of Colloid and Interface Science*, v. 26, n. 1, p. 62–69.
673   https://doi.org/10.1016/0021-9797(68)90272-5

675   **Tay, Q.; Liu, X.; Tang, Y.; Jiang, Z.; Sum, T. C.; Chen, Z. 2013.** Enhanced
676   photocatalytic hydrogen production with synergistic two-phase anatase/brokite TiO_2
677   nanostructures. *The Journal of Physical Chemistry*, v.117, p.14973-14982.
678   https://doi.org/10.1021/jp4040979

679

680 **Veras, T. S.; Mozer, T. S.; Santos, D. C. R. M.; Cesar, A. S. 2018**. Hydrogen: Trends,
681 production and characterization of the main process worldwide. *International Journal of*
682 *Hydrogen Energy*, v. 42, n. 4, p. 2018-2033.
683 https://doi.org/10.1016/j.ijhydene.2016.08.219
684
685 **Yin, S.; Ihara, K.; Liu, B.; Wang, Y.; Li, R.; Sato, T. 2007.** Preparation of anatase,
686 rutile and brookite type anion doped titania photocatalyst nanoparticles and thin films.
687 *Physica Scripta*, v. 129, p. 268-273. https://doi.org/10.1088/0031-8949/2007/T129/060
688
689
690

Figure 1

Infrared transmission spectra obtained for the synthesized oxides.

Infrared transmission spectra obtained for the synthesized oxides.
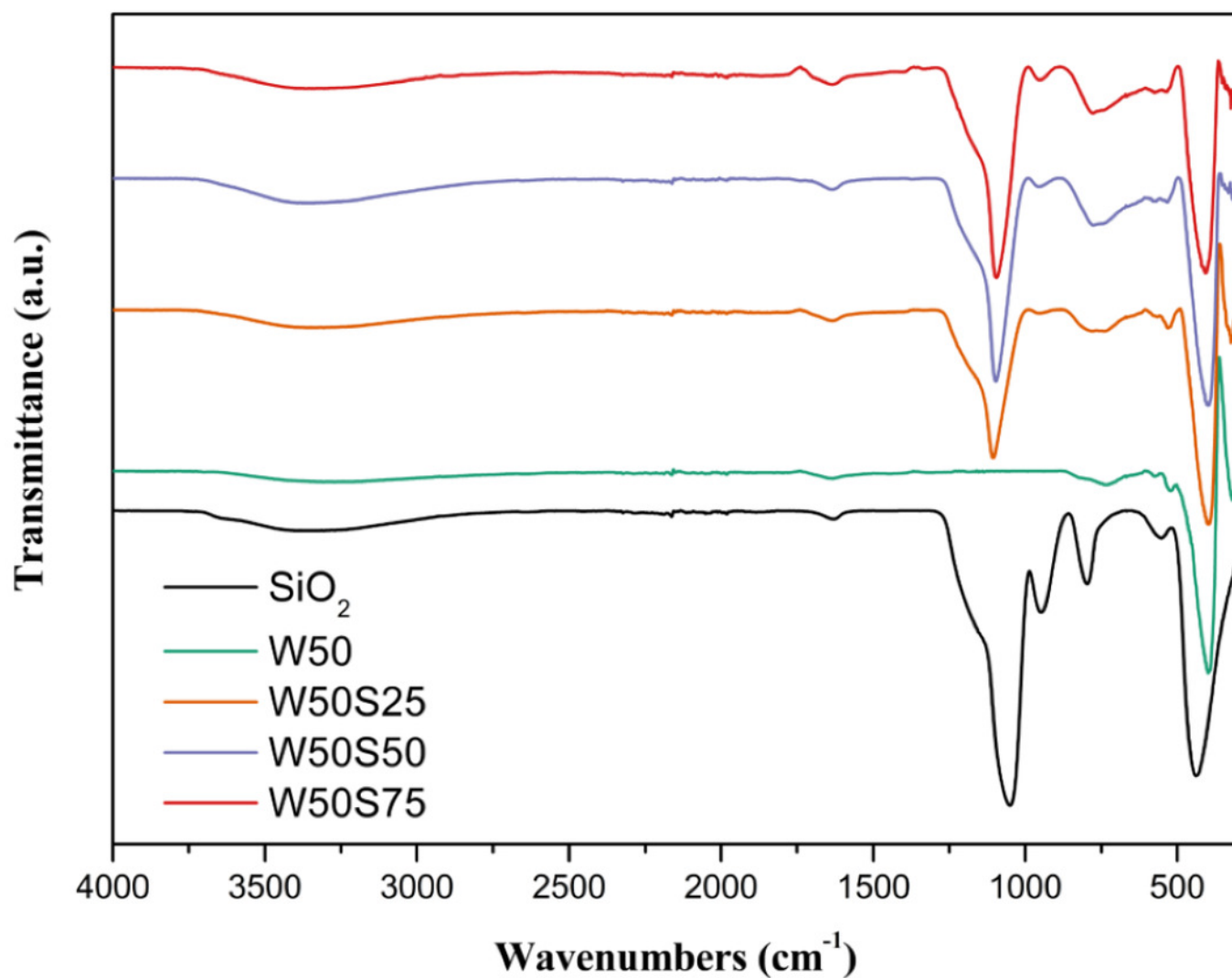
Figure 2

X-ray diffractogram for the synthesized oxides.

X-ray diffractogram for the synthesized oxides.
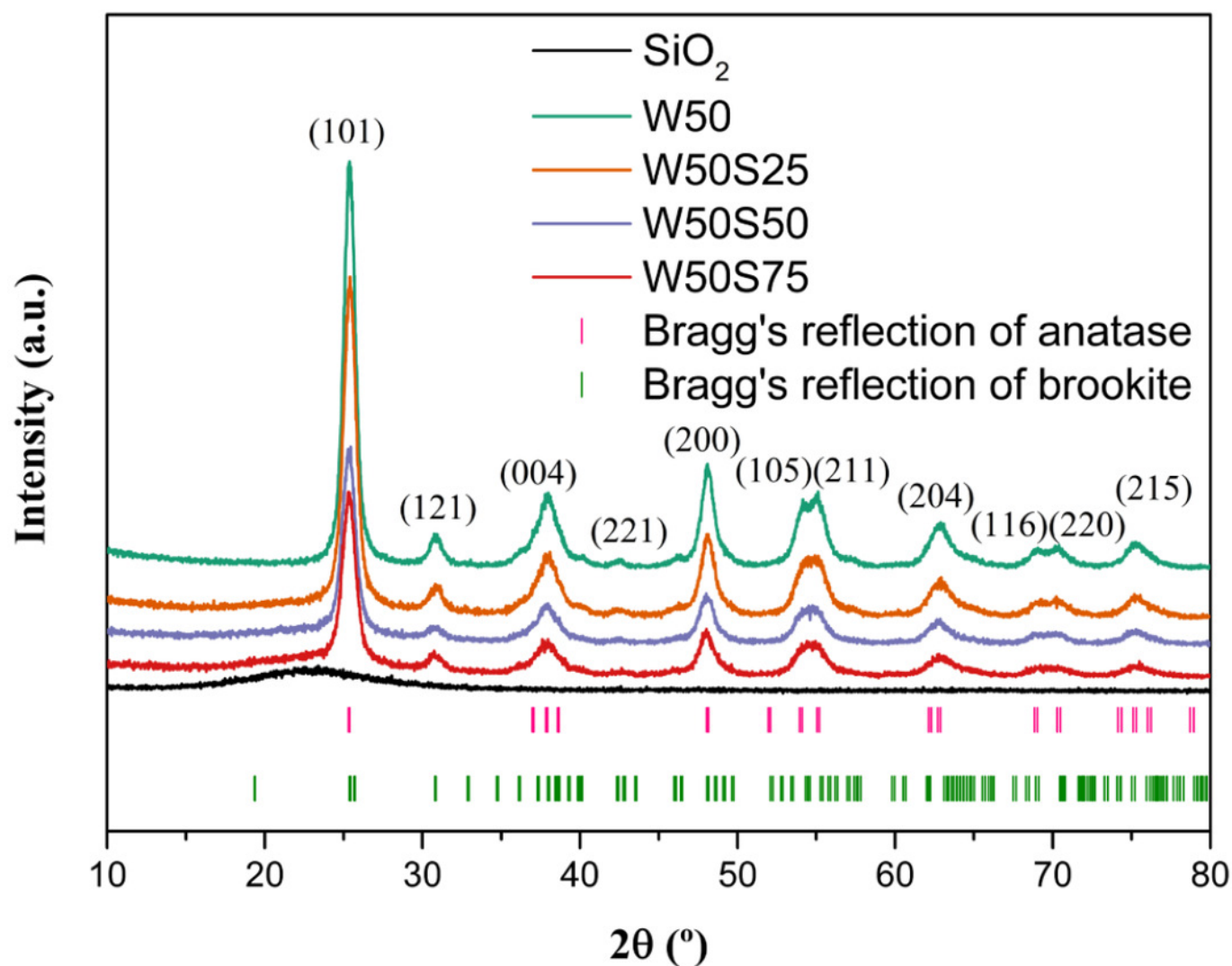
Figure 3

Raman spectra of the synthesized materials. Insert: bands at 245 cm^{-1}, 321 cm^{-1}, 365 cm^{-1} and 452 cm^{-1}, attributed to brookite phase.

Raman spectra of pure TiO_2 and composites. In detail, the signals attributed to brookite phase.
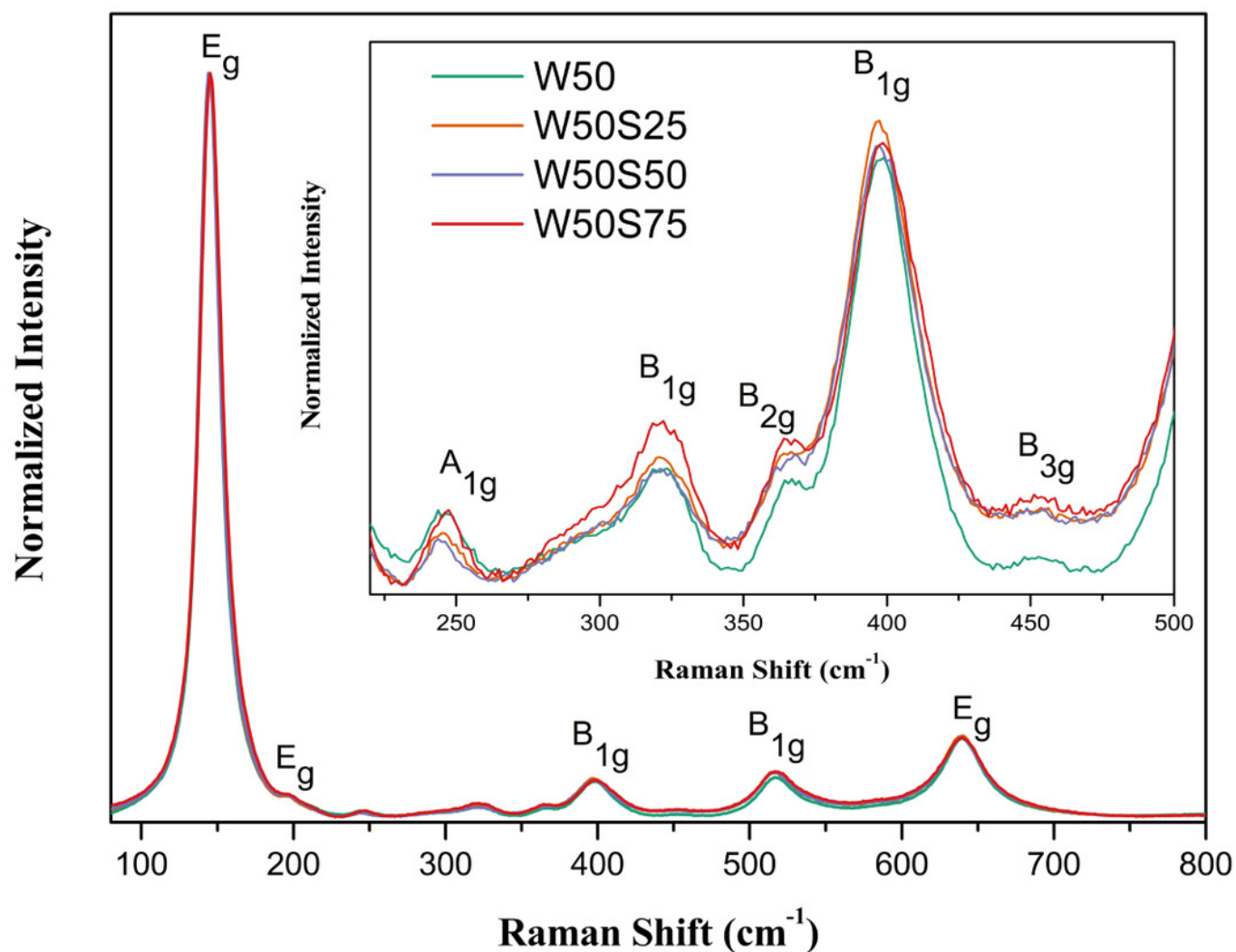
Figure 4

Diffuse reflectance spectra in an enlarged scale vs. Kubelka-Munk's function, combined to linear segments used in determining E_g values. Insert: Diffuse reflectance spectra, without magnification, for the synthesized materials.

Diffuse reflectance spectra of SiO_2 and composites.
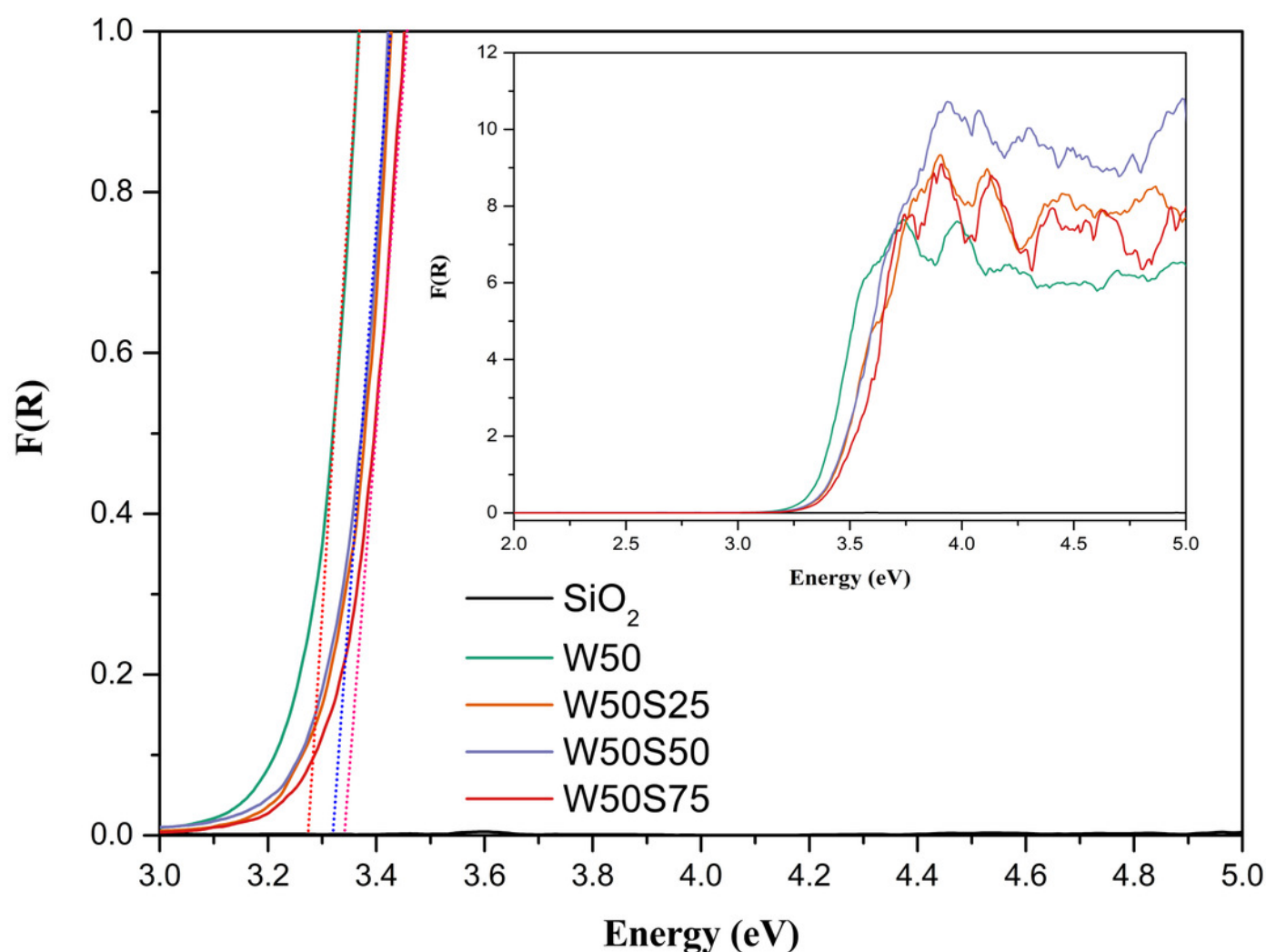
Figure 5

Photocatalytic production of hydrogen vs. Reaction time for the materials under study.

Photocatalytic production of hydrogen vs. reaction time, for SiO_2 and composites.
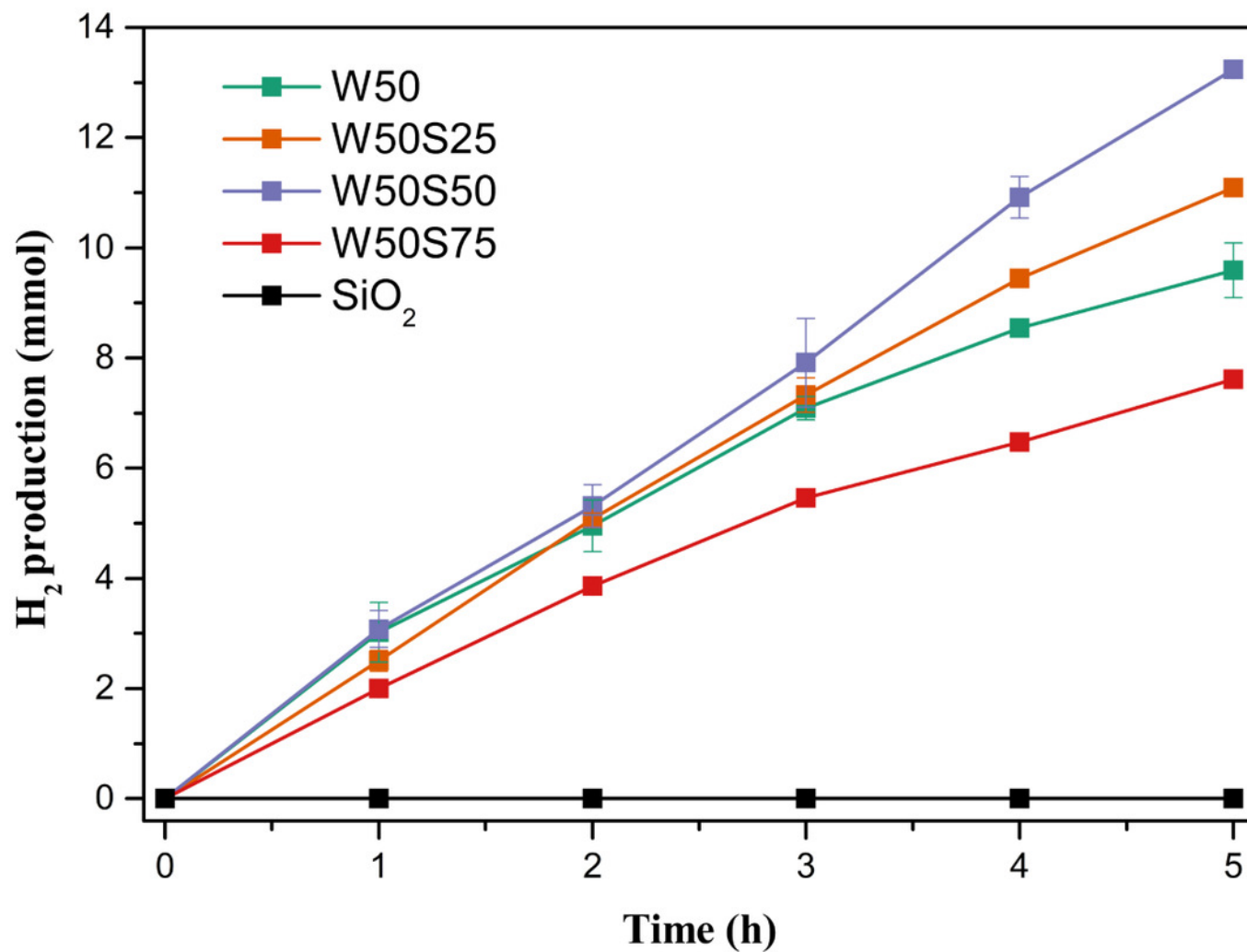
Figure 6

Amount of H_2 produced by the photocatalyst W50S50 in four cycles of reuse.

Amount of H_2 produced by the photocatalyst W50S50 in different cycles of reuse.
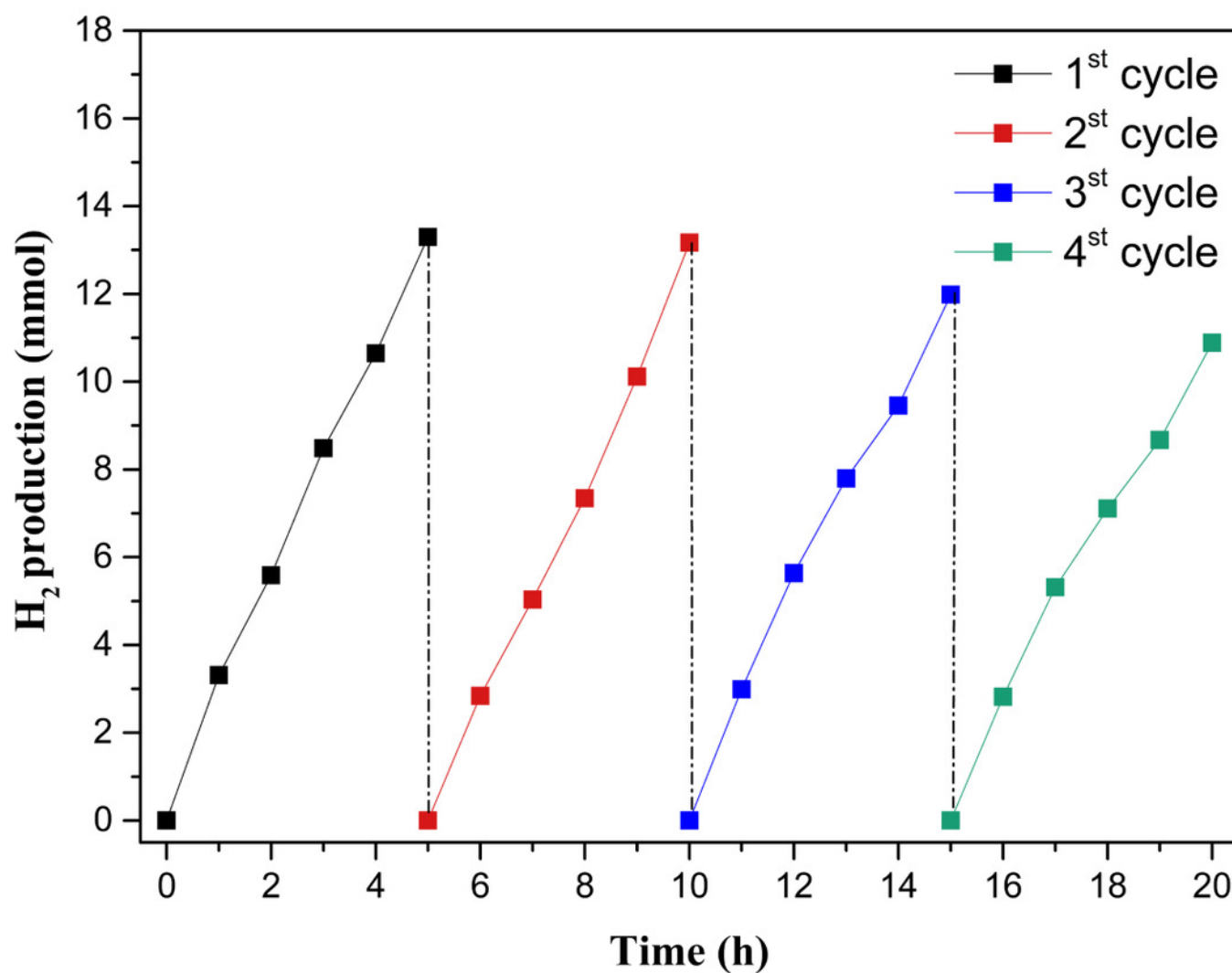
Figure 7

Amount of H$_2$, in µmols, produced by the photocatalysts W50 and W50S50, using a solar simulator.

Amount of H$_2$, in µmols, produced by the photocatalysts W50 and W50S50, using a solar simulator.
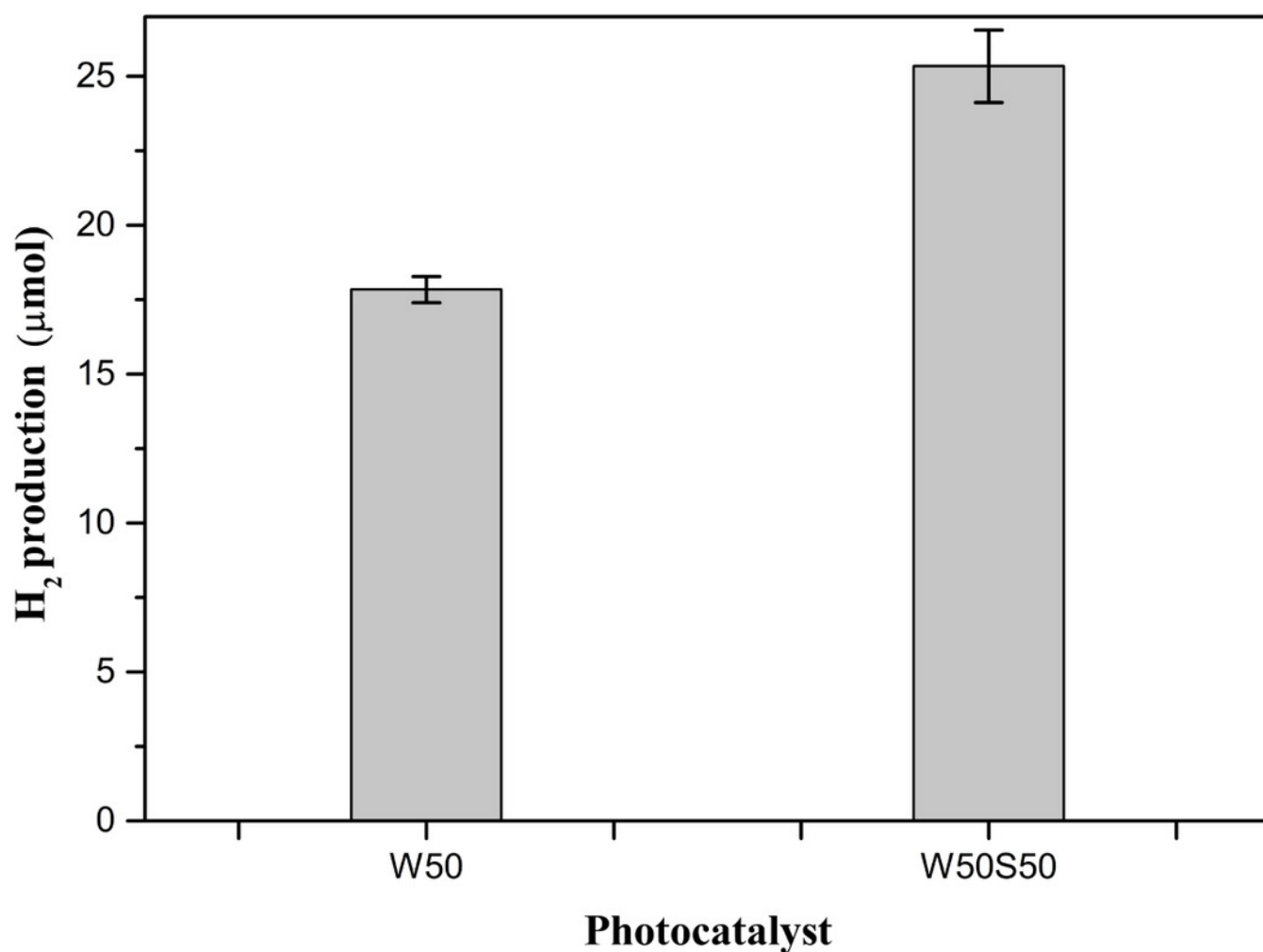
Morphological parameters related to the synthesized materials.

Morphological parameters related to SiO_2, TiO_2 and composites.

Table 1- Morphological parameters related to the synthesized materials.

Photocatalyst	Average particle size (µm)	Surface area (m^2/g)	Porosity (%)	Mean pore diameter (nm)
W50	0.7 – 1.0	103	16.5	6.0
W50S25	0.5	130	19.5	6.0
W50S50	0.4	120	21.0	7.0
W50S75	0.4	113	20.5	8.0
SiO$_2$	0.2	42.0	5.0	4.0

Percentage of crystalline phase, size and average maximum crystallite deformation, obtained from Rietveld refinement.

Percentage of crystalline phase, size and average maximum crystallite deformation, obtained from Rietveld refinement, for TiO_2 and composites.

Table 2- Percentage of crystalline phase, size and average maximum crystallite deformation, obtained from Rietveld refinement.

Photocatalyst	Crystal phase (%)		Mean size of crystallite (nm)	Average maximum crystallite deformation (%)
W50	Anatase	76.0	32	9
	Brookite	24.0	14	10
W50S25	Anatase	75.5	27	12
	Brookite	25.5	15	12
W50S50	Anatase	70.0	22	13
	Brookite	30.0	9	19
W50S75	Anatase	73.0	6	15
	Brookite	27.0	10	23

Amount, in mmol of H_2, produced, specific rate of H_2 production (SRHP), initial and final pHs for each cycle in the reuse assay.

Amount, in mmol of H_2, specific rate of H_2 production (SRHP), initial and final pHs per cycle, in the reuse assay.

Table 3 - Amount, in mmol of H_2, produced, specific rate of H_2 production (SRHP), initial and final pHs for each cycle in the reuse assay.

Cycle	n (mmols)	SRHP (mmol $h^{-1}g^{-1)}$	Initial pH	Final pH
1st	13.5	32.0	6.17	5.78
2nd	13.0	31.0	6.20	5.38
3rd	12.0	28.5	6.15	4.45
4th	11.0	26.0	6.15	4.30